








**Impact of electron capture rates for nuclei far from stability on core-collapse supernovae**Aurélien Pascal <sup>1,\*</sup> Simon Giraud <sup>2,†</sup> Anthea F. Fantina <sup>2,‡</sup> Francesca Gulminelli <sup>3,§</sup> Jérôme Novak <sup>1,||</sup>  
Micaela Oertel <sup>1,¶</sup> and Adriana R. Raduta <sup>4,#</sup><sup>1</sup>*LUTH, Observatoire de Paris, PSL Research University, CNRS, Université Paris Diderot, Sorbonne Paris Cité,  
5 Place Jules Janssen, 92195 Meudon, France*<sup>2</sup>*Grand Accélérateur National d'Ions Lourds (GANIL), CEA/DRF - CNRS/IN2P3, Boulevard Henri Becquerel, 14076 Caen, France*<sup>3</sup>*LPC (CNRS/ENSICAEN/Université de Caen Normandie), UMR6534, 14050 Caen Cédex, France*<sup>4</sup>*National Institute for Physics and Nuclear Engineering, RO-077125 Bucharest, Romania*

(Received 9 June 2019; revised manuscript received 28 August 2019; published 15 January 2020)

The impact of electron-capture (EC) cross sections for neutron-rich nuclei on the dynamics of core collapse during infall and early post-bounce is studied by performing spherically symmetric simulations in general relativity using a multigroup scheme for neutrino transport and full nuclear distributions in extended nuclear statistical equilibrium models. We thereby vary the prescription for EC rates on individual nuclei, the nuclear interaction for the equation of state, the mass model for the nuclear statistical equilibrium distribution, and the progenitor model. In agreement with previous works, we show that the individual EC rates are the most important source of uncertainty in the simulations, while the other inputs only marginally influence the results. A recently proposed analytic formula to extrapolate microscopic results on stable nuclei for EC rates to the high densities and temperatures and the neutron-rich region, with a functional form motivated by nuclear-structure data and parameters fitted from large scale shell-model calculations, is shown to lead to a sizable (16%) reduction of the electron fraction at bounce compared to more primitive prescriptions for the rates, leading to smaller inner core masses and slower shock propagation. We show that the EC process involves  $\approx 170$  different nuclear species around  $^{86}\text{Kr}$ , mainly in the  $N = 50$  shell closure region, and establish a list of the most important nuclei to be studied in order to constrain the global rates.

DOI: [10.1103/PhysRevC.101.015803](https://doi.org/10.1103/PhysRevC.101.015803)**I. INTRODUCTION**

Much effort has been devoted for decades to numerical simulations of core-collapse supernovae (CCSN), and a lot of progress has been achieved toward understanding the complex physics of these spectacular events (see, e.g., [1,2]). But even if the main processes have been elucidated, many details still deserve attention.

It was first pointed out by Bethe *et al.* [3] and confirmed by many subsequent studies that electron capture (EC) on nuclei plays an important role during the late stages of stellar evolution and the prebounce phase of CCSN [4–8]. For very close CCSN, the Deep Underground Neutrino Experiment (DUNE) [9] might even be able to detect neutrinos from the prebounce phase, as an indicator of EC reactions [10]. Most sophisticated simulations of CCSN evolution thereby model EC in inhomogeneous nuclear matter typically by considering

a nuclear statistical ensemble (NSE) distribution of nuclei together with microscopically calculated EC rates [11].

Different recent works have, however, pointed out that our understanding of these processes under relevant thermodynamic conditions is still insufficient and has an impact on the dynamics of core collapse [12–17]. In particular, the systematic study by Sullivan *et al.* [12] has shown that the uncertainties on the EC rates on individual nuclei induce stronger modifications to the mass of the inner core at bounce and the maximum of the neutrino luminosity peak than the progenitor model or the equation of state (EoS).

The results of Ref. [12] and the subsequent study [18] clearly indicate that the simulations are most sensitive to the EC rates for neutron-rich nuclei near the  $N = 50$  closed shell and, to less extent, near the next closed shell at  $N = 82$ . The main difficulty is that for the relevant nuclei not much information is available, either experimental or from microscopic calculations. The situation is nevertheless expected to improve in the near future due to dedicated research programs and theoretical efforts (e.g., [19,20]). Several other works have highlighted other aspects. First of all, total EC rates are influenced as much by the nuclear distribution given by the EoS as by the rates on individual nuclei, with both suffering from uncertainties. Uncertainties in matter composition mainly stem from the definition of clusters in a hot nuclear environment and nuclear properties far from the

\* aurelien.pascal@obspm.fr

† giraud@ganil.fr

‡ fantina@ganil.fr

§ gulminelli@lpccaen.in2p3.fr

|| jerome.novak@obspm.fr

¶ micaela.oertel@obspm.fr

# araduta@nipne.ro

stability valley. Uncertainties in rates on individual nuclei are mainly due to nuclear structure and finite temperature effects. The sensitivity of EC rates to the former was addressed in Refs. [13,14,16]. Raduta *et al.* [13] showed that the unknown binding energies of nuclei far beyond the stability valley and a possible shell quenching might increase the total EC rate by up to 30%. Nuclear abundances also influence the neutrino opacity via neutrino-nucleus scattering [14]. Future experiments with exotic beams might improve the situation in that respect, but further work is necessary. Nagakura *et al.* [17] point out that a consistent treatment of nuclear abundances in the EoS and for calculating weak interaction rates is important to correctly study the EoS dependence of both the dynamics and neutrino signals.

Concerning the individual rates, mostly values from microscopic calculations—where available [11,21–25]—have been used. By far the richest collection of microscopically calculated EC rates is discussed by Juodagalvis *et al.* [11]. In particular, in order to be able to extend the calculations to heavier and more neutron-rich nuclei populated abundantly in the later stages of collapse, the authors define a strategy to describe electron captures by a hierarchy of nuclear models. However, although this seminal work of Juodagalvis *et al.* [11] is used by some groups performing CCSN simulations, the data are not publicly available. The analytic parametrization of Ref. [26] is designed to complement microscopic data for high electron densities and temperatures and is extensively used in simulations and also to calculate rates for nuclei not present in the databases.

It has to be emphasized that the nuclei identified in Refs. [12,18] as having the highest impact lie outside the region where—apart from the work by Juodagalvis *et al.* [11]—microscopic calculations exist. Although we await more microscopic calculations and additional information from charge-exchange experiments (which, e.g., should correctly include additional Pauli blocking effects [18]), in Ref. [15] an extended analytic parametrization has been proposed incorporating different physical effects at high electron density, temperature, and isospin ratio with the aim of improving the reliability of the extrapolation to regions not covered by microscopic calculations. It has been shown that the improved parameterization leads to a systematic reduction of the total EC rate, in agreement with expectations [18], which can reach one order magnitude for some thermodynamic conditions.

In Refs. [13,15], the impact of a potential shell quenching and of the improved EC rate parametrization on the prebounce evolution of core collapse has been illustrated using some typical thermodynamic conditions with EC rates added perturbatively. Here we will perform self-consistent core-collapse simulations investigating the effect of modified EC rates and the mass model on the evolution. In contrast to Ref. [12], where individual EC rates were globally scaled by arbitrary factors ranging from 2 to 10 with respect to the fiducial values, we show here the effect of a physically motivated reduction of EC on nuclei. For easier use of our improved model in simulations, we will provide total EC rates and neutrino-nucleus scattering opacities for the employed EoS within the CompOSE database [27], with a numerically efficient format easily adaptable to any EoS.

The paper is organized as follows. We start by specifying the setup of our simulations in Sec. II. In Sec. III we discuss the influence of different ingredients on the infall and early post-bounce evolution. In addition to comparing the different prescriptions for the EC rates on individual nuclei, we investigate the dependence on the progenitor model and on the EoS, including different nuclear interaction models and different mass models for determining binding energies of neutron-rich nuclei. Section IV is devoted to a determination of the most relevant nuclei for EC in order to specify the nuclei for which microscopic and/or experimental studies are the most needed. We conclude in Sec. V.

## II. SETUP OF THE SIMULATIONS

### A. General description

In order to perform self-consistent numerical simulations of CCSN, we use two different hydrodynamic codes in general relativity. Most results are obtained with the spherically symmetric version of the CoCoNuT code [28]. It solves the general-relativistic (GR) hydrodynamics, with a  $3+1$  decomposition of spacetime. High-resolution shock-capturing schemes are used for hydrodynamic equations, whereas the Einstein equation for the gravitational field is solved with spectral methods [29]. In addition to the five evolution equations solved for hydrodynamics (coming from the conservation of baryon current and energy-momentum tensor), this model considers the advection equation for the electron fraction  $Y_e = n_e/n_B$ , where  $n_e$  and  $n_B$  are the electron and baryon number densities, respectively.

The source terms for neutrino energy losses and depletion are computed using the “fast multigroup transport” scheme developed by Müller and Janka [30]. This scheme solves the stationary neutrino transport in the ray-by-ray approximation, with a closure relation for the first Eddington factor. In the collapse phase the first Eddington factor is set to 1, which is equivalent to a free-streaming condition. In the post-bounce phase the closure is obtained from a two-stream approximation as in [30]. We switch between these two closures relations at neutrinosphere detection (when the central optical depth becomes larger than 0.66).

The analyses of the mass model and the most relevant nuclei in Secs. III B 4 and IV require the use of a very flexible input for the EoS and the matter composition. This is most easily achieved by employing the perturbative approach of Ref. [31]. For simplicity, this has not been implemented in the CoCoNuT code, which works with tabulated versions of the EoS, but is in an improved version of the code developed in Refs. [32–34], called ACCEPT in the following. This spherically symmetric code uses the same techniques for solving GR hydrodynamics as CoCoNuT. The differences between the codes in solving Einstein equations are negligible within our CCSN prebounce context. Neutrinos are treated in a simple leakage-type scheme with a multigroup treatment: they are considered either fully trapped (inside the neutrinosphere) or freely streaming (outside the neutrinosphere), the neutrinosphere being defined by a trapping density parameter. This parameter has been adjusted such that both codes

produce compatible results for all observables shown in this paper, except the neutrino luminosity, leading to a value of  $10^{12} \text{ g cm}^{-3}$ . Due to the obvious limitations of the leakage scheme in ACCEPT, the neutrino luminosity cannot be well reproduced within this scheme. This does, however, not affect the results of Secs. III B 4 and IV. We have checked that the limitation of the neutrino source terms to charged-current reactions in ACCEPT is irrelevant for the results presented in those sections, too. Finally, in all the simulations presented here, initial models (progenitor star) come from publicly available data computed by Woosley *et al.* [35].

### B. Equations of state

During the different stages of the core-collapse evolution, wide domains of density ( $10^{-12} \lesssim n_B \lesssim 1 \text{ fm}^{-3}$ ), temperature ( $0.1 \lesssim k_B T \lesssim 50 \text{ MeV}$ ), and charge fraction ( $0.01 \lesssim Y_e \lesssim 0.6$ ) are explored. Matter consists of baryons, leptons (electrons, positrons, neutrinos, and antineutrinos) and photons, and it has a homogeneous/inhomogeneous structure at supra-/subsaturation densities. Leptons and photons interact weakly and are usually treated as ideal Fermi and, respectively, Bose gases. Composition and thermodynamics of baryonic matter is still under study, because of the uncertainties related to the effective interactions and difficulties in the modeling.

The most intensively used EoS models so far [36,37] employ the so-called single nucleus approximation (SNA). It describes baryonic matter at subsaturation densities as a mixture of a uniform distribution of self-interacting nucleons, a free gas of  $\alpha$  particles, and a unique cluster of nucleons, all of which are in thermal and chemical equilibrium with respect to the strong interaction. Interactions between unbound nucleons and nuclear clusters are included via the classical excluded volume approximation and in-medium modifications of cluster surface energy. The shortcoming of this approach becomes obvious at high temperature, where the macroscopic thermal equilibrium state corresponds to a collection of distinct microscopic states. The SNA is known to have only a negligible impact on thermodynamic quantities [38], but it could affect the weak interaction rates, which are highly sensitive to structure effects, and thus finally impact the astrophysical evolution [39].

A more sophisticated approach consists of employing an extended nuclear statistical equilibrium (NSE) model which accounts for the entire nuclear distribution. Several NSE models and resulting EoS have been proposed in the last decade; see, e.g., [39–45]. For the interaction between nucleons, different relativistic mean field models, Skyrme effective interactions, or variational approaches have been employed that span significant ranges of nuclear matter parameters in both isovector and isoscalar channels, accounting well for present day uncertainties in the nuclear matter EoS. Here we are mainly interested in the infall phase, i.e., matter at subsaturation densities and with moderate isospin asymmetries. Consequences of the above uncertainties in the nuclear interactions on stellar matter are small in this regime, since a significant amount of matter is bound in clusters and, by construction, all effective interactions offer a fair description of ground state nuclei. More important differences among

the different NSE models arise from the modeling of nuclear clusters via the treatment of (i) (thermally) excited states, (ii) maximum allowed isospin asymmetry, (iii) nuclear level density, and (iv) nuclear binding energies away from the valley of stability, where no experimental data exist. It has been shown that the last point strongly influences the nuclear abundances under the thermodynamic conditions during collapse [13,14]. Additional differences exist in the identification of the bound and unbound parts of nuclear clusters to define abundances, but this point did not sizably modify the EoS [42]. For further details, the reader is referred to [40,42].

For this work, as a fiducial case we will consider the NSE model of [40] with DD2 [46] relativistic mean field effective interaction; see Hempel *et al.* [39]. This model takes into account the ensemble of nuclei whose masses have been calculated within the finite range droplet model by Moller *et al.* [47]. To get an idea of EoS effects, we will consider a second model, the NSE EoS of [41]. It employs the SLy4 [48] Skyrme effective interaction. Nuclear clusters have  $2 < A < 300$  and, in principle, any value of the isospin asymmetry. Their binding energies are complementarily given by experimental data [49,50], the predictions of the ten-parameter model by Duflo and Zuker [51], and a liquid drop model parameterization [52], with parameters harmonized with SLy4.

Finally, in order to assess the effect of shell closures far from stability, we will compare different models for the nuclear masses, using the perturbative method described by Grams *et al.* [31] build upon on the EoS by Lattimer and Swesty [36]. Specifically, the already mentioned phenomenological Duflo and Zuker mass model [51] (DZ10), which imposes the same magic numbers irrespective the isospin asymmetry, will be compared with the Brussels-Montreal microscopic mass model<sup>1</sup> HFB-24 [55]. The latter, based on the self-consistent Hartree-Fock-Bogoliubov method, uses a 16-parameter generalized Skyrme effective nucleon-nucleon interaction with a realistic contact pairing force, and predicts a considerable quenching of the  $N = 50$  shell gap far from stability [55]. Both DZ10 and HFB-24 provide an excellent reproduction of measured masses, with a root-mean-square deviation of about 0.5 MeV with respect to the 2012 Atomic Mass Evaluation [50]. We will consider, too, as an extreme case, masses as described by the compressible liquid drop model (CLDM) of the Lattimer-Swesty EoS [36], which completely neglects shell effects.

### C. Electron capture rates

The rate of a generic weak interaction reaction (electron and positron capture and  $\beta$  decays) depends—apart from physical constants—on the nuclear transition strength and a phase space factor. At finite temperature weak reactions involve several states in the parent and daughter nuclei, such that nuclear structure effects enter the transition strength via both nuclear energy levels and transition matrix elements. Different reaction channels can contribute to the latter. In most

<sup>1</sup>The mass table for this model is available in the BRUSLIB database [53]; see also Ref. [54].

cases, it is dominated by Fermi (vector) and Gamow-Teller (axial) contributions. The phase space factor depends on the electron capture reaction kinematics and takes the form of integrals over the momenta of incoming and outgoing particles [56]. As such, it shows strong dependence on thermodynamic conditions.

The first systematic calculation under stellar conditions is due to Fuller, Fowler, and Newman [21,56–58], who have also made available [21] the first weak interaction rate table for nuclei with masses between 21 and 60 for a large grid of temperature  $T$  and electron density  $n_e$ :  $10^{-3} \leq k_B T \leq 10$  MeV and  $10^{-14} \leq n_e \leq 10^{-3} \text{ fm}^{-3}$ .

The fact that astrophysical simulations require high-accuracy weak interaction rates motivated further extensive microscopic calculations optimized on experimental data, considering in general the same  $T$ - $n_e$  grid as Fuller *et al.* [21]. Different techniques have been employed, ranging from large scale shell-model (LSSM) calculations [22,24,59] to the random-phase approximation [60,61] and quasiparticle random-phase approximation (QRPA) [62,63]. By accounting for all possible correlations among valence nucleons in a major shell, LSSM calculations offer the most accurate microscopic description available to date, as testified by their ability to reproduce the measured Gamow-Teller (GT) distributions, lifetimes, and low energy spectroscopy [64]. They exist for  $sd$ - ( $17 \leq A \leq 39$ ) [24] and  $fp$ -shell nuclei ( $45 \leq A \leq 65$ ) [22,59]. The mass domain  $65 \leq A \leq 80$  is covered by the table of Ref. [25], which employs an empirical approach. Finally, weak interaction rate tables for  $sd$ -,  $fp$ -, and  $fp$ -shell nuclei with  $18 \leq A \leq 100$  are given in [62,63], which employ QRPA. QRPA was also recently employed in [19] for calculating EC rates of neutron-rich nuclei with  $26 \leq Z \leq 41$  and  $75 \leq A \leq 93$ , which correspond to the high-sensitivity region of Ref. [18]. Hybrid models which use shell-model Monte Carlo (SMMC) [65] or Fermi-Dirac parametrizations [11] to determine the population of excited states and RPA techniques for weak interaction rates have also been proposed and exploited to extend the existing data to heavier and more neutron-rich nuclei. In this way, the work by Juodagalvis *et al.* [11] contains information for nuclei with  $66 \leq A \leq 120$  (250 nuclides) and with  $28 \leq Z \leq 70$  and  $40 \leq N \leq 160$  (2200 nuclides). In particular, cross-shell correlations which are important to overcome the  $N=40$ , 50, and 82 shell gaps are accounted for, in agreement with the results of finite temperature SMMC. Moreover, based on the observation that the electron Fermi energy grows faster with core density than the nuclear  $Q$  value, Juodagalvis *et al.* [11] define a strategy to describe electron captures by a hierarchy of nuclear models. They provide NSE-averaged EC rates along two collapse trajectories. These rates are not appropriate for other studies where the nuclear distribution is calculated consistently from the employed EoS.

It is easy to see that the available databases cover a finite mass domain and an isospin asymmetry range close to the valley of stability. Although strong structure effects translate into EC rates that, for low temperatures and electron density, can vary by more than one order of magnitude between neighboring nuclei in the isotopic chart, the need for estimates for other nuclei, including the neutron-rich ones copiously

populated during the late collapse stages, and/or thermodynamic conditions out of the grids, lead to the use of extrapolations and approximations within simulations.

The first parametrization, proposed by Bruenn [66], relies on the independent particle model and estimates the GT matrix element by the number of protons in the  $\pi 1f_{7/2}$  shell and the number of neutron holes in the  $\nu 1f_{5/2}$  one. The reaction  $Q$  value entering the phase space factor is approximated by the difference between proton and neutron chemical potentials. This prescription results in the total suppression of EC on both light and/or neutron-rich nuclei, which is certainly unrealistic.

An improved parametrization, which is presently the most extensively used in CCSN simulations, was proposed in Langanke *et al.* [26]. It is based on results of SMMC calculations at finite temperature in the full  $pf$ - $sdg$  shell with residual pairing plus quadrupole interactions and RPA calculations of EC for nuclei with  $65 \leq A \leq 112$ . At variance with the independent particle model, all nuclei studied by Langanke *et al.* [26] manifest holes in the  $pf$  shell and, for  $Z > 30$ , nonvanishing proton occupation numbers in the  $sdg$  orbitals. This means that GT transitions are unblocked and EC rates take place. This new parametrization reads

$$j^{\text{EC}} = \frac{\ln 2\mathcal{B}}{K} \left( \frac{k_B T}{m_e c^2} \right)^5 [F_4(\eta) - 2\chi F_3(\eta) + \chi^2 F_2(\eta)]. \quad (1)$$

In this expression,  $\chi = (Q - \Delta E)/k_B T$ ,  $\eta = \chi + \mu_e/k_B T$ , where  $Q$  denotes the EC reaction heat,  $Q = M(A, Z)c^2 - M(A, Z-1)c^2$ , with  $M(A, Z)$  the nuclear mass and  $\Delta E = E_f - E_i$ .  $m_e$  and  $\mu_e$  stand for electron rest mass and chemical potential, respectively.  $F_i(\eta)$  denotes the relativistic Fermi integral,  $F_i(\eta) = \int_0^\infty dx x^i / [1 + \exp(x - \eta)]$ .  $\mathcal{B}$  represents an average value for the nuclear matrix element and  $K$  is a characteristic time. The constant values proposed in Ref. [26],  $\mathcal{B} = 4.6$ ,  $\Delta E = 2.5$  MeV, and  $K = 6146$  s, are obtained from a fit of SMMC + RPA calculations for nuclei with  $65 \leq A \leq 112$ , and are shown to correctly reproduce their gross features for the thermodynamic conditions explored for the central element before bounce [26]. For lower values of temperature and electron density, Eq. (1) may nevertheless lead to both underestimations and overestimations of microscopic calculations, as shown in Refs. [26,67]. Note that the parameter  $\Delta E$  accounts for possible transitions from and to excited states in the parent/daughter nucleus, so that it is not necessary to introduce an effective  $Q$  value such as that by Sullivan *et al.* [12].

The above parametrization, Eq. (1), being integrated over neutrino energies, cannot actually be implemented directly into our multigroup neutrino treatments. Instead we use the following expression for the neutrino creation rate ( $\Theta$  is the usual Heaviside step function and  $f_{e^-}$  the electron distribution function):

$$j(\epsilon) = \Theta(\epsilon - \chi k_B T) \frac{\ln 2\mathcal{B}}{K} \left( \frac{1}{m_e c^2} \right)^5 \frac{(hc)^3}{4\pi c} \times (\epsilon - \chi k_B T)^2 f_{e^-}(\epsilon - \chi k_B T), \quad (2)$$

which, once integrated over neutrino energy  $\epsilon$  assuming a vanishing neutrino distribution function, exactly reproduces

Eq. (1). Throughout this work this parametrization will be denoted LMP (Langanke–Martínez-Pinedo).

Equation (1) was recently generalized by Raduta *et al.* [15], allowing for temperature, electron density, and isospin  $I = (N - Z)/A$  dependence as well as for odd-even effects in  $\Delta E$ . The temperature dependence contains two competing effects: the increasing number of excited states in the daughter nucleus with increasing temperature, leading to a larger  $\Delta E$ ; and the decreasing electron chemical potential,  $\mu_e$ , for fixed electron density, which shows the opposite trend. With increasing  $n_e$ , more excited states and higher energies can be populated and thus  $\Delta E$  increases, too. Finally the isospin dependence and odd-even effects of  $\Delta E$  are introduced to account for nuclear structure effects in the centroid of the GT resonance, as computed within LSSM for  $pf$ -shell nuclei [59].

As shown in Ref. [15] for a wide range of thermodynamic conditions typical of late stage evolution of core collapse, the most important improvement of Eq. (1) arises from isospin and odd-even effects, i.e., nuclear structure properties. These features are particularly useful in accounting for the large dispersion of  $j^{\text{EC}}$  in a given  $Q$ -value bin—as shown by the data in [22,24,25,62,63]—and for the extrapolation to large negative  $Q$ , typical of intermediate mass neutron-rich nuclei [15]. In relation to the latter effect we point out that, for  $k_B T \gtrsim 1$  MeV and the highest  $n_e$  values considered in the grid, the improvements discussed by Raduta *et al.* [15] lead to EC rates lower by two orders of magnitude or more than those produced assuming Eq. (1). Given the overall neutron enrichment of stellar matter before bounce, reduction of two orders of magnitude of the individual rates on neutron-rich nuclei entails a reduction of up to one order of magnitude for the average EC rate summed over the complete nuclear distribution [15]. Further developments, which are out of the scope of present work, should also account for isospin effects on the GT strength [59] and temperature-dependent Pauli blocking.

Out of the different improved versions of Eq. (1) proposed in [15] we shall here consider only one, model 3, which best reproduces microscopic data. To be more precise, instead of employing a global value  $\Delta E$ , for each grid point of  $n_e(i)$ ,  $T(j)$  in the microscopic calculations we write

$$\Delta E^{(AB)}(n_e(i), T(j)) = b_{i,j}^{(AB)} I + c_{i,j}^{(AB)}, \quad (3)$$

and intermediate values of  $n_e$ ,  $T$  are obtained by linear interpolation. The coefficients  $b$ ,  $c$  were determined by Raduta *et al.* [15] by a least-squares fit to LSSM calculations. Equation (3) assumes a linear isospin dependence and odd/even effects are included by employing different coefficients  $\{(AB)\} = \{(OO), (OE), (EE)\}$  for odd-odd, odd-even, and even-even nuclei, respectively. For details and in particular values of the coefficients, see the Appendix of Raduta *et al.* [15]. Hereafter this isospin dependant parametrization, implemented in its energy dependent form Eq. (2), will be referred to as ISO.

During the advanced stage of the collapse, before  $\beta$  equilibrium is reached at the center of the star,  $T$  and  $n_e$  exceed the values covered by the weak rate tables and thus  $\Delta E$  cannot be fitted in that region. We have used two different ways to extrapolate  $\Delta E$  in this case: (i) first-order extrapolation or (ii)

TABLE I. Progenitor models taken from Woosley *et al.* [35]. Mass at collapse denotes the mass present on the numerical grid at the beginning of simulation.

Progenitor name	Metallicity	ZAMS mass	Mass at collapse
s15	Solar	$15M_\odot$	$2.1M_\odot$
s25	Solar	$25M_\odot$	$2.9M_\odot$
s40	Solar	$40M_\odot$	$2.6M_\odot$
u15	$10^{-4} \times \text{Solar}$	$15M_\odot$	$2.0M_\odot$
u25	$10^{-4} \times \text{Solar}$	$25M_\odot$	$2.3M_\odot$
u40	$10^{-4} \times \text{Solar}$	$40M_\odot$	$4.6M_\odot$

constant value fixed to the last available  $T$ ,  $n_e$  grid point. The predicted EC rate (and subsequently the evolution of  $Y_e$ ) differ by less than 3.5 % between these two procedures, indicating that EC rates under those extreme conditions are of little relevance and that the extrapolation procedure for  $\Delta E$  is not of great influence.

A word of caution has to be added. Being based on fits of  $pf$ -shell nuclei, the approximation proposed in Ref. [15] might not be appropriate for EC rates of heavy nuclei, which, due to cross-shell correlations, manifest suppression of Pauli blocking effects [68]. This unblocking of the GT transition was predicted by theoretical models for nuclei with  $Z < 40$  and  $N > 40$ , and confirmed by experiments.

### III. EVOLUTION OF THE COLLAPSE

All simulations start from an unstable stellar model as mentioned in Sec. II A. Except for Sec. III B 3, where we study the influence of the progenitor model on the results, a  $15M_\odot$  progenitor from Woosley *et al.* [35], the s15 model, will be used; see Table I. We then follow the collapse of the iron core, with establishment of  $\beta$  equilibrium at the center, and finally stop the simulation a few milliseconds after bounce. Simulations in Secs. III A to III B 2 were performed with the CoCoNuT code, whereas those in Secs. III B 4 and IV were done with the ACCEPT code.

#### A. Influence of electron capture rates

Our fiducial simulation starts from a  $15M_\odot$  progenitor (zero-age main sequence) labeled s15 in the catalog by Woosley *et al.* [35]. As a first test we plot in Fig. 1 averaged EC rates in the central cell of our numerical grid, as functions of the baryon density in that cell during infall, for all three approaches detailed in Sec. II C: the original one by Bruenn [66], LMP [26], and ISO [15]. To average the rates, we assume a Fermi-Dirac equilibrium distribution for neutrinos,

$$j_{\text{av}} = \int_0^\infty j(\epsilon) \epsilon^3 f_\nu^{\text{(eq)}}(\epsilon) d\epsilon. \quad (4)$$

The density where  $\beta$  equilibrium is achieved with the different EC prescriptions is shown by dashed lines. From this figure it is obvious that, up to a baryon density of  $n_B \simeq 2 \times 10^{-5} \text{ fm}^{-3}$ , EC rates given by Bruenn's model are higher than the LMP and ISO ones. The behavior gets inverted at densities between  $2 \times 10^{-5} \text{ fm}^{-3}$  and  $7 \times 10^{-4} \text{ fm}^{-3}$  because, within this density interval, many neutron-rich nuclei are

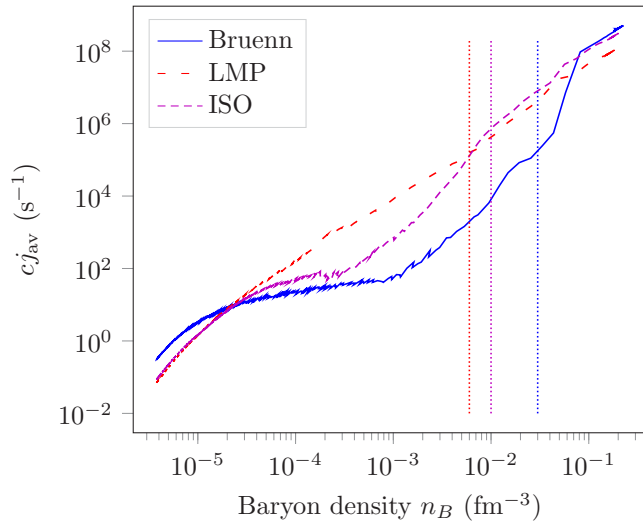


FIG. 1. EC rate evolution (labeled by baryon density) in the central grid cell during infall using different prescriptions for the EC rate on nuclei; see text for details. The vertical dashed lines show the density above which  $\beta$  equilibrium sets in.

populated with vanishing EC rates in the simplified Bruenn approach. This density region is located close to the onset of  $\beta$  equilibrium with the highest EC rates, such that it is to be expected that the difference in EC rates between the three models is relevant for the evolution. The importance of EC on neutron-rich nuclei has already been noted in Ref. [7], where the predictions of simulations employing Bruenn’s rates have been compared with those obtained by simulations in which EC rates have been implemented according to shell-model and hybrid shell-model–RPA calculations (for about 200 nuclei with  $45 \leq A \leq 112$ ) and the LMP formula.

The electron fraction  $Y_e$  is directly linked to the EC rates. Its time evolution at the center of the star is plotted in Fig. 2. During infall, the model with Bruenn’s rates shows a different behavior with respect to the LMP and ISO models. This can be understood as follows: during most of the collapse, the central baryon density is lower than  $2 \times 10^{-5} \text{ fm}^{-3}$  and EC rates by Bruenn are higher than the other ones (see Fig. 1), which implies a lower  $Y_e$  for the model using Bruenn’s EC rates before  $t \simeq 210$  ms. As shown in Fig. 1, for higher densities until the onset of  $\beta$  equilibrium, the situation is inverted and EC rates by LMP and ISO models are higher, leading to a stronger decrease of  $Y_e$  after  $t \simeq 210$  ms. This behavior shows again the importance of EC rates in the density range  $2 \times 10^{-5} \leq n_B \leq 7 \times 10^{-4} \text{ fm}^{-3}$  for the evolution of the collapse, where EC on neutron-rich nuclei occurs. At bounce, differences of about (30%) in  $Y_e(r=0)$  are observed, which can be explained by the fact that EC in this density region occurs predominantly on nuclei for which no microscopic calculations exist [12]. Regarding the predictions of the LMP and ISO models, one notes that differences occur only for  $t \gtrsim t_{\text{bounce}} - 30$  ms and they are less than 20%, with LMP providing the strongest decrease of  $Y_e$ .

The study by Sullivan *et al.* [12]—where, in order to account for uncertainties in EC rates, these are scaled by a

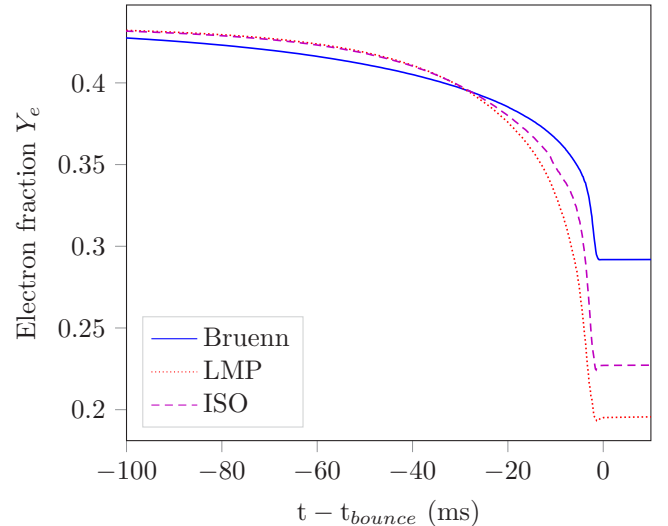


FIG. 2. Time evolution of the electron fraction  $Y_e(r=0)$  for the central element of the numerical grid for all three EC models during the late prebounce phase.

constant factor of 10—indicates differences of up to  $\pm 30\%$  in the central  $Y_e$  at bounce. The nuclear physics considerations (mainly isospin dependence and odd-even effects; see Sec. II C) entering the improved model ISO considerably reduce the EC rates in the late stages of collapse and thus clearly point to a higher  $Y_e$  at bounce than LMP.

In Figure 3 we display the radial  $Y_e$  profiles at bounce for the three EC rate models. These results indicate that differences appear mostly in the central region of the collapsing star, i.e., for  $r \lesssim 50$  km at bounce, where neutron-rich nuclei are most abundant. As the three EC rate models presented in this paper mostly differ on these exotic nuclei, the overall behavior displayed in Fig. 3 is understandable.

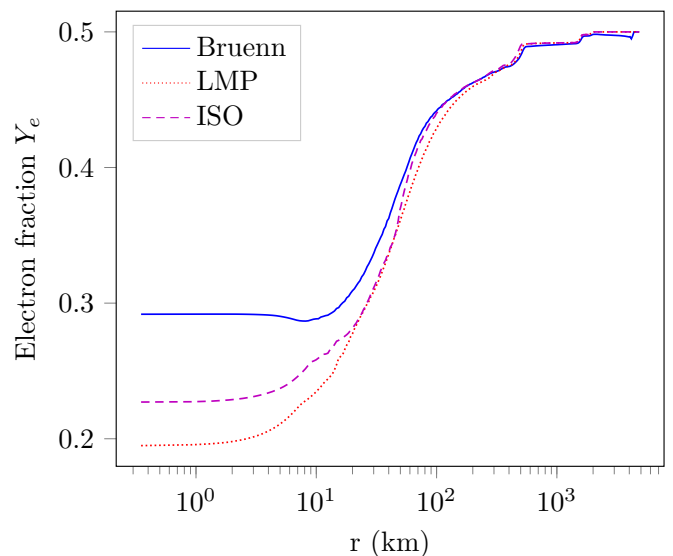


FIG. 3. Radial profiles of the electron fraction at bounce employing the three different EC rate prescriptions.

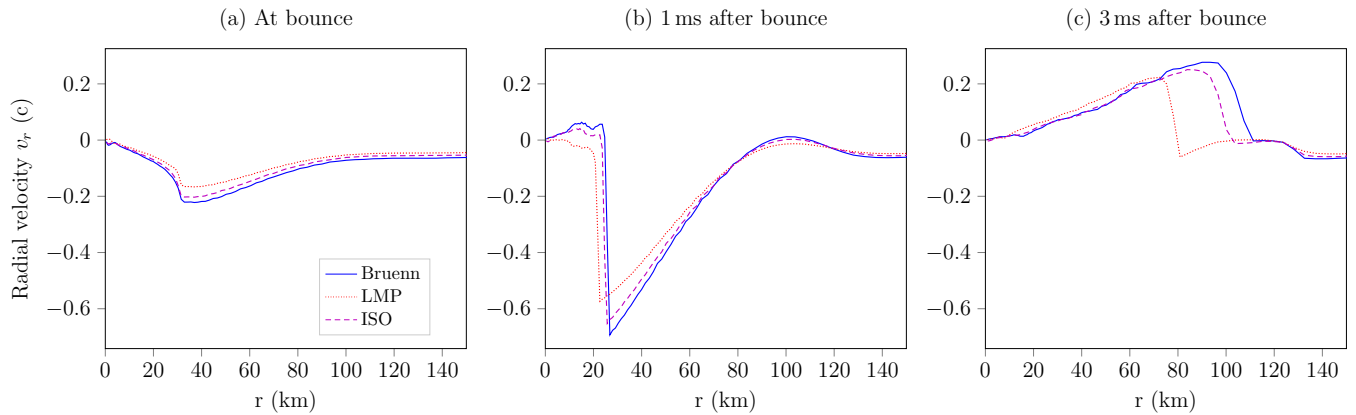


FIG. 4. Comparison of shock propagation at different instants during the early post-bounce phase with the three different EC rate prescriptions.

Going further, we now look at the influence of our EC rate models on the collapse and bounce dynamics. Since the collapse can be seen essentially as a free fall, it is clear that the collapse time shows only little difference between the models: it is about 4% larger with the LMP and ISO models than with Bruenn's rates. This small difference can be understood from the fact that, in the early collapse phase, electron degeneracy pressure is dominant. The lower electron fraction for the model with Bruenn's rates (see Fig. 2) in this phase thus explains the accelerated collapse.

Radial velocity profiles at bounce, and at two instants after bounce (1 and 3 ms) are shown in Fig. 4. Although the radius at which the shock is formed is the same for all three EC rate models (left panel), the situation is different 3 ms after bounce (right panel), where the shock is seen to have reached the largest distance from the center for the Bruenn case, and is closest to the center with the LMP rates. This can be interpreted in terms of the inner core mass, i.e., the mass of the matter inside the shock formation radius: the higher the mass of this inner core, the larger the kinetic energy given to the shock. Additionally, if the inner core mass is larger, the iron layers that must be crossed by the shock are thinner, thus making the shock lose less energy. Values of the inner core mass at bounce are computed to be  $0.31M_{\odot}$ ,  $0.4M_{\odot}$ , and  $0.45M_{\odot}$ , for models with EC rates from LMP, ISO, and Bruenn, respectively, confirming the above reasoning. Please note that, if we had shown the shock position as a function of the enclosed mass and not as a function of the radius (left panel of Fig. 4), the difference in the inner core mass at bounce would have induced visible differences; see, e.g., Fig. 7 of Sullivan *et al.* [12].

The ordering of the inner core mass can in turn be understood as a consequence of the electron fraction evolution discussed above: The mass of the inner core at bounce is roughly proportional to  $\langle Y_{L(e)}^2 \rangle$ , the mean fraction of trapped leptons squared [69], which is fixed and given by  $Y_e$  at the moment when neutrino trapping sets in.

Finally, Fig. 5 illustrates the time evolution of electron neutrino luminosity a few ms before and after bounce. For all considered EC rate models two peaks are obtained. The first peak corresponds to roughly 1 ms before bounce, while

the second corresponds to 2–4 ms after bounce. The steep electron neutrino luminosity increase before bounce is due to the increase of electron captures on protons bound in nuclei, whose fraction is augmented as the density increases. At about 1 ms before bounce the core density reaches the neutrino trapping density. As a consequence, the luminosity decreases. The process lasts about 2 ms, until the shock reaches the neutrinosphere and the neutrino flux increases again. Regarding the peak amplitudes, a significant dependence on the EC rate model is to be noticed. The relative ordering of the peaks—the same before and after bounce—is nevertheless counter-intuitive: the smallest (Bruenn)/largest (LMP) EC rates produce the highest/lowest amplitudes. According to Ref. [12], where this dependence was noticed for the first time, the explanation relies on two effects. First, low opacities, caused by low EC rates, allow the neutrinosphere to move to inner radii. Second, large inner cores favored by low EC rates

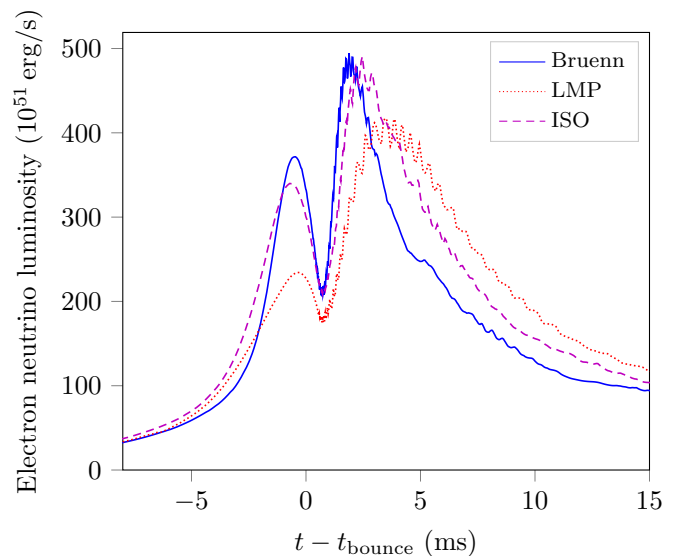


FIG. 5. Time evolution of electron neutrino luminosity around bounce, for the three different EC rate prescriptions.

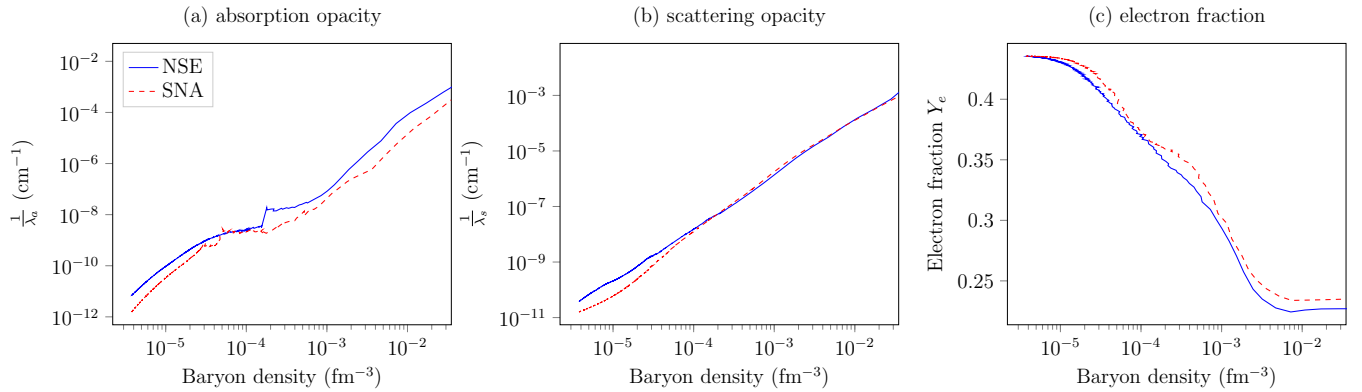


FIG. 6. Neutrino inverse mean free path as functions of baryon density in the central numerical cell with reactions computed either on a single mean nucleus (SNA) or on a statistical ensemble of nuclei (NSE): contribution of electron capture effects only (left panel) and scattering effects only (central panel). Electron fraction time evolution for both models (right panel).

are more efficient in transferring energy to the shock which consequently propagates outwards faster. The velocity profiles given in Fig. 4 confirm this interpretation.

The total energy taken away by electron neutrinos, up to 15 ms after bounce, can be computed and is roughly independent of the EC rate model:  $4.58 \times 10^{51}$  erg with Bruenn's model,  $4.90 \times 10^{51}$  erg with LMP, and  $4.99 \times 10^{51}$  erg with ISO.

## B. Influence of other parameters

### 1. SNA vs NSE

We study here the influence of other parameters on the infall evolution, starting with a comparison between NSE or SNA approaches within the EoS (see Sec. II B for details) when computing neutrino reactions. To that end, we simulate infall using EC rates computed with the ISO model, the s15 progenitor model, as well as the HS(DD2) EoS. SNA calculations thereby extract the average nucleus from the entire available NSE distribution. Thermodynamic quantities are thus unchanged between SNA and NSE and we can more easily isolate neutrino reaction effects. In the SNA case, the  $Q$  value needed for both LMP and ISO models is computed using the nucleus obtained by rounding off the average ( $A, Z$ ) to the closest integers.

This approach differs from previous studies comparing SNA and NSE prescriptions. Studies focusing on thermodynamic quantities of course recalculate the full EoS in the SNA or NSE approach, but employ in general simplified neutrino treatments; see, e.g., Hempel *et al.* [39], who calculate the NSE weak reactions extracting two average nuclei from the full distribution with Bruenn rates. They confirm that considering the full nuclear distribution for thermodynamic quantities has only a minor impact [39,70] on core collapse. In contrast, the importance of taking into account the full nuclear distribution for calculating weak rates is well known; see, e.g., [7]. Our approach allows us to properly investigate the issue since we consistently compute weak rates from the nuclear distribution of the underlying EoS.

The left panel of Fig. 6 shows a comparison of averaged neutrino inverse mean free paths from EC processes in the

central cell,

$$\frac{1}{\lambda_a} = \int_0^\infty \kappa_a^*(\epsilon) \epsilon^3 f_v^{(\text{eq})}(\epsilon) d\epsilon / \int_0^\infty \epsilon^3 f_v^{(\text{eq})}(\epsilon) d\epsilon, \quad (5)$$

as a function of baryon density.  $\kappa_a^*$  denotes here the absorption opacity corrected for stimulated absorption given by  $j(\epsilon)/f_v^{(\text{eq})}$  [66]. This Fermi-Dirac weighted average yields the correct mean free path for gray energy transport in an optically thin medium. As expected, most important differences appear in the density ranges above  $n_B \gtrsim 10^{-4} \text{ fm}^{-3}$ , where the nuclear distribution is large and potentially dominated by more than one peak.

The middle panel of Fig. 6 shows a comparison of NSE and SNA for the averaged inverse neutrino mean free path obtained from scattering off nuclei. We assume isoenergetic scattering and include corrections due to ion correlations and electron screening; see Horowitz [71] and Bruenn and Mezzacappa [72] for detailed expressions. The right panel shows the time evolution (labeled by baryon number density) of  $Y_e$  in the central cell for both cases.

It is obvious that, although differences between SNA and NSE occur mainly in the region where the nuclear distribution is large, the overall effect is much smaller than when using different prescriptions for EC rates. We should stress, however, that Bruenn's rates as well as both LMP and ISO parametrizations average over nuclear structure effects, and the difference between NSE and SNA might become more important when employing microscopic rates all over the nuclear chart, which are presently not available.

### 2. EoS dependence

The EoS model can have some influence on the electron fraction, too. To check this, we compare simulations obtained with both extended NSE EoS models described in Sec. II B: HS(DD2) from Hempel *et al.* [39] and the SLy4 from Raduta and Gulminelli [42] using model ISO for the EC rate.  $Y_e$  at the star's center shows little differences during the collapse, and almost no difference in the resulting value at onset of  $\beta$  equilibrium and at bounce. For the evolution of the central density after bounce, only small differences between the two



models were noted, too. The only noticeable discrepancy between the two EoS models could be seen in the temperature evolution at the center of the star: the EoS by Raduta and Gulminelli [42] always leads to slightly lower values than the one by Hempel *et al.* [39], but these differences have little influence on the overall dynamics during prebounce and early post-bounce.

The EoS dependence of the CCSN evolution before and after bounce was previously considered in Refs. [12,17,39,73,74], which employed a relatively wide collection of models in both SNA and NSE frameworks. The unanimous conclusion is that a certain, though limited, dependence is observed for practically all considered thermodynamic and dynamic quantities in all stages of the evolution as well as for the deleptonization rate,  $Y_e$ , and neutrino signals. Fischer *et al.* [74] reached the conclusion that  $Y_e$  of the protoneutron star and its evolution depend on the symmetry energy.

### 3. Progenitor dependence

We have also explored the role of the progenitor model in the determination of electron fraction at bounce by considering six different models from Woosley *et al.* [35]; see Table I. The simulations employ ISO EC rates and the HS(DD2) EoS. Although the overall collapse time may noticeably depend on the type of progenitor, with differences of up to 25%, the electron fraction at bounce varies only from 0.23 to 0.27, with the exception of the model u40, for which it drops down to 0.2. This last point can be understood from the large mass present on the numerical grid at the beginning of the collapse (see Table I). We thus confirm conclusions from Sullivan *et al.* [12], who showed that the detailed progenitor model can have less influence on the electron fraction at bounce than the precise EC rate prescription.

### 4. Influence of the nuclear mass model

Finally, we have examined the influence of the nuclear mass model on the dynamics of the collapse. Previous works [13,14,31] have shown that the composition of matter in the thermodynamic conditions of core collapse considerably varies according to the functional used for extrapolating nuclear masses beyond known ones. In particular, since the composition is dominated by magic nuclei [12], it was reported in Refs. [13,14,31] that a potential modification of magicity far from stability would strongly affect the distribution of matter.

For the present study, we have used the perturbative method introduced in Ref. [31] to compute the NSE distribution starting from a given density functional for the EoS. As mentioned in Sec. II B, the Lattimer-Swesty functional has been applied for that purpose and simulations have been performed with the ACCEPT code using the LMP parametrization for the EC rates.

In Fig. 7 the evolution of the most probable nucleus as a function of time in the central element is shown, comparing the predictions from a CLDM prescription (by Lattimer and Swesty, LS [36]), with that of two microscopic mass models, DZ10 [51] and HFB-24 [55]. In very good qualitative agreement with Refs. [13,31], we can see that the presence (in

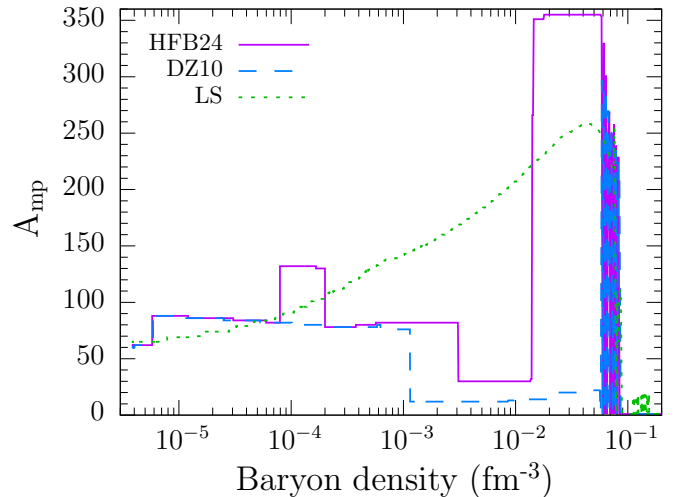


FIG. 7. Baryonic number of the most probable nucleus in the central element during infall as a function of time (labeled by the baryon number density). Three different mass models are considered.

DZ10 and HFB-24) or absence (in LS) of shell effects impacts in a considerable way the composition of matter. The HFB-24 model, which predicts a stronger quenching of the shell gaps far from stability than the DZ10 model, naturally predicts a faster evolution towards heavier nuclei. This is expected, since a quenching of the shell gap reduces the waiting-point effect due to magicity, well known in the framework of  $r$ -process calculations [75].

However, the differences between the mass models only marginally affect the global dynamical evolution of the collapse. This is demonstrated in Fig. 8, which gives as an example the radial profile at bounce of different representative quantities. The behavior of the most probable cluster (left part) follows the trends already observed in Fig. 7. Since a potential magicity quenching does not change the global pattern of nuclei produced, but only the time at which they appear, it is not surprising that the profiles at bounce of the different models are very similar. Less expected is the fact that the electron fraction and entropy profile (central and right parts of Fig. 8) of the different models are indistinguishable, meaning that the time integrated effect of the different compositions is very small. This is true even for the simplistic liquid drop model (LS), which does not account for any structure effect, and even if the global distribution of nuclei is very different between the LS and the other models at all times (see Fig. 6 of Ref. [31]). This is clearly noticeable in Fig. 9 (see also Fig. 6 of Ref. [31]),<sup>2</sup> where

<sup>2</sup>The nuclear distributions shown in Fig. 9 appear to be quite different from those shown in Fig. 6 of Ref. [31]. This is because in Ref. [31] the cluster probabilities have been calculated on a fixed core-collapse trajectory using Bruenn's rates and with a trapping density fixed to  $3 \times 10^{11} \text{ g cm}^{-3}$ , while here the calculations have been consistently done in the core-collapse simulations using LMP rates and a trapping density fixed at  $10^{12} \text{ g cm}^{-3}$ , thus yielding different thermodynamic conditions.

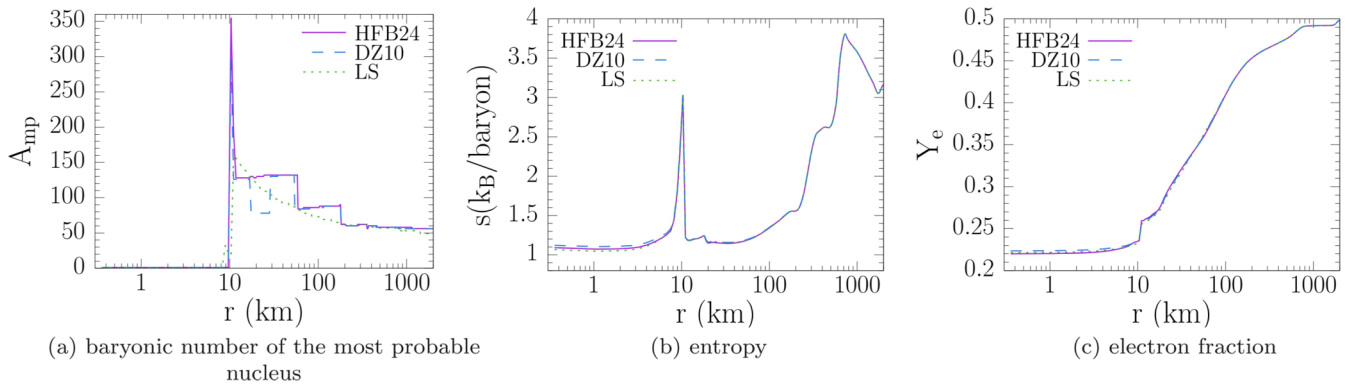


FIG. 8. Radial profile at the time of bounce of the baryonic number of the most probable nucleus (left), the entropy (central), and the electron fraction (right), using three different mass models.

we plot the distribution of nuclei for a given thermodynamic condition reached during the collapse in the center of the star ( $k_B T = 1$  MeV,  $\rho_B = 6.02 \times 10^{11}$  g cm $^{-3}$ ,  $Y_e = 0.27$ ) for the LS model (oval-shaped contours) and the HFB-24 mass model (bimodal contours). While for the LS model the most probable nucleus is located around  $N \approx 86$  and  $Z \approx 37$ , for the HFB-24 mass model the most probable nucleus is still located around the magic number  $N = 50$  and  $Z = 28$ , and the probabilities show a bimodal distribution with a second peak close to the magic number  $N = 82$ .

This might be at least partially explained by the fact that for this simulation we have used an analytic continuous parametrization (LMP) for the EC rates, washing out nuclear structure effects observed in microscopic rate calculations [22]. Some dependence on the different mass models might therefore be recovered if microscopic rates consistent with the mass model were used. Unfortunately, this cannot be tested presently since, as we show in the next section, the number of nuclear species present in the tabulated microscopic rates

is largely insufficient to cover the NSE distribution and in particular the relevant nuclei for EC during collapse. However, even if a final quantitative conclusion cannot be drawn at present, it is clear from Fig. 8 that the details of the mass model have much less influence on the dynamics of core collapse than precise EC rates.

#### IV. DETERMINATION OF THE MOST RELEVANT NUCLEI

In the previous section we showed that the most influential microscopic ingredient entering a core-collapse simulation is the expression of the individual EC rates, particularly their behavior at low  $Q$  values, which corresponds to very neutron-rich nuclei and which is still largely unknown. The improved parametrization ISO, providing a better fit to the microscopic calculations by Langanke and Martinez-Pinedo [22], suggest a considerable average reduction of the rates in the neutron-rich region with respect to the original parameterization LMP. Still, the difference observed in the collapse dynamics arises from the extrapolation of those fits to unknown regions where neither data nor microscopic calculations are available. It is therefore clear that additional constraints are needed at low  $Q$  values before a parametrization can be considered fully reliable. For this reason, here we try to identify the most important nuclei for the deleptonization process. Experiments and/or microscopic calculations on these key nuclei could provide benchmarks for future improved parametrizations.

The simulations of this section were performed with the same settings as in Sec. III B 4, employing the HFB-24 [55] mass model.

An estimation of the number of nuclear species that should be taken into account to have a realistic core-collapse simulation can be inferred from Fig. 10. In the upper part we display the deleptonization rate obtained by considering only the  $k$  most abundant nuclei in the NSE distribution, as a function of the number  $k$  of considered nuclei. The reason why we prefer to rank nuclei according to their abundances rather than the more relevant product between abundance and capture rate is that the latter quantity is strongly affected by the assumed EC rate model. The different curves are labeled by their instantaneous EC rate, which is a monotonically rising function of time, and the different curves correspond thus to different times during collapse, before reaching  $\beta$

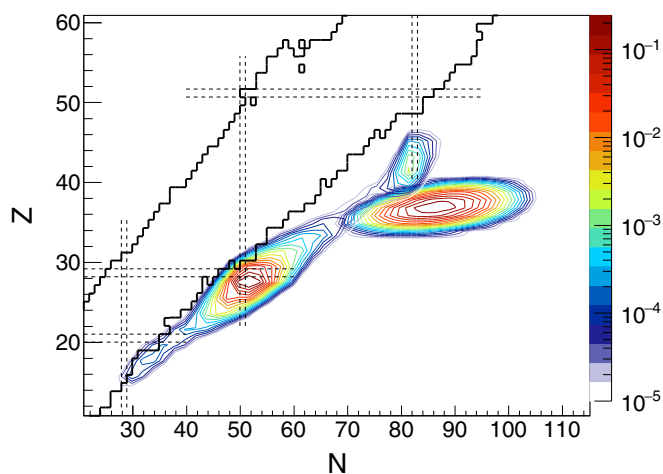


FIG. 9. Distribution of nuclei ( $N, Z$ ) for a chosen thermodynamic condition during the collapse before trapping:  $k_B T = 1$  MeV,  $\rho_B = 6.02 \times 10^{11}$  g cm $^{-3}$ ,  $Y_e = 0.27$ . Contour lines correspond to the cluster normalized probabilities (red to blue, more to less probable) for the original LS model (oval-shaped contour) and for the HFB-24 nuclear mass model. See text for details.

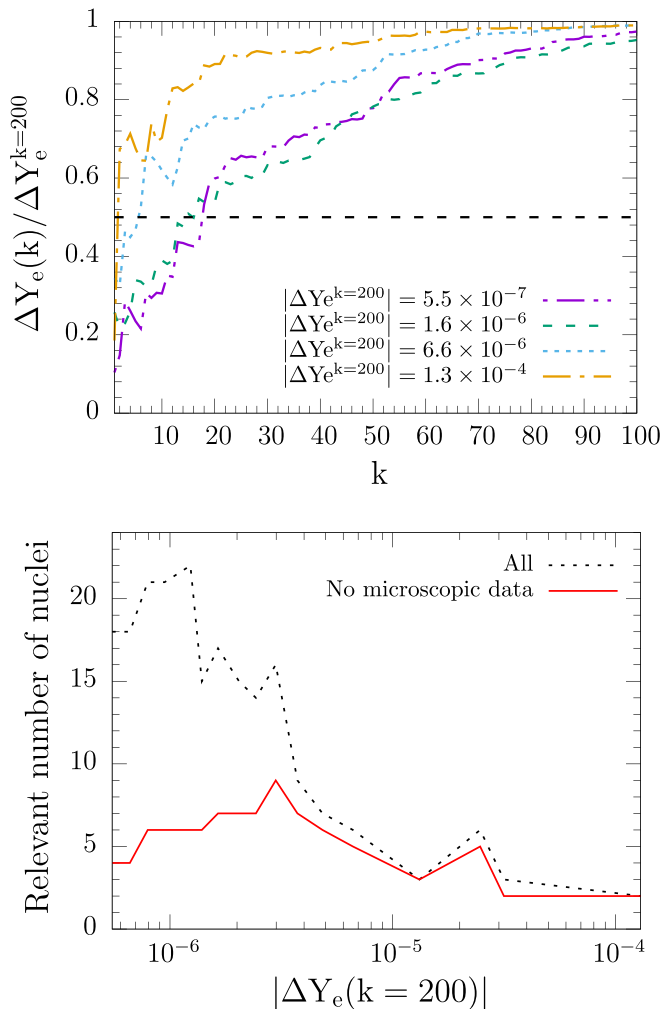


FIG. 10. Upper panel: the instantaneous capture rate evaluated on a limited number  $k$  of nuclei, normalized to the rate obtained taking the 200 most probable ones, as a function of the size of the sample. Nuclei are ordered according to their abundance. The labels give the instantaneous rate on the whole distribution, with lower rates corresponding to earlier times. Lower panel: the number of nuclei accounting for 50% of the total instantaneous rate is plotted as a function of the EC rate (dashed line). The number of species which are not included in the tabulated microscopic EC rates [21,22,24,25] is plotted with a solid line.

equilibrium. The rate is normalized to the value obtained by summing the contribution of the 200 most abundant nuclei, considering that  $k = 200$  is sufficient at all times to recover the total rate.

The SNA approximation, obtained considering  $k = 1$  in Fig. 10 (upper part), obviously leads to a systematic underestimation of the rate by a factor between 2 and 10, depending on the time. As observed in Fig. 6, this underestimation leads to roughly 5% overestimation of the electron fraction at bounce, meaning that a larger pool of nuclei has to be considered at each time step to have a complete picture of the collapse.

To get an idea of how many different nuclei have to be considered, we display in the lower part of Fig. 10 the number of nuclei responsible for half of the total EC rate as function

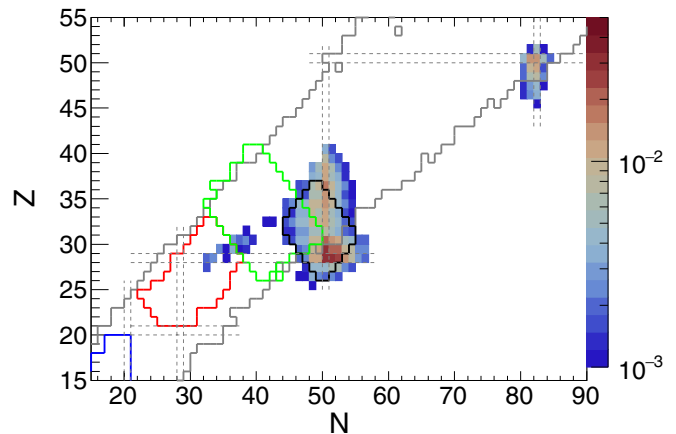


FIG. 11. Time integrated relative deleptonization rate (color scale) associated to the different nuclear species identified by their proton  $Z$  and neutron  $N$  number. The black contour indicates the most relevant nuclei for EC identified by Sullivan *et al.* [12] and Titus *et al.* [18]. The red, blue, and green contours indicate the nuclei for which microscopic rates are available from Langanke and Martinez-Pinedo [22], Oda *et al.* [24], and Pruet and Fuller [25], respectively. Nuclei with experimentally known masses are situated between the gray lines.

of time (labeled by the total instantaneous rate). It shows that at each time one-half of the total rate is due to the capture on not more than 20 nuclei, which decreases to less than 5 in the later stages before  $\beta$  equilibrium is reached and EC and its inverse  $\beta$  decay become irrelevant.

We show in the same figure the number of those relevant nuclei for which microscopic calculations [21,22,24,25] are not available (solid line). Evidently, for many nuclei contributing in a dominant way to EC during collapse, no microscopic rates exist. In particular in the later stages, most relevant for the dynamics of the collapse, the rates on all those nuclei have to be estimated by extrapolations. Note, however, that the number of relevant unconstrained rates is relatively limited. The corresponding isotopes are represented in Fig. 11, where the color scale represents the relative contribution to the time integrated rate associated with the different nuclei. The ensemble of nuclei represented in this figure account for 89% of the total time integrated EC rate, and can therefore be considered as the relevant pool of nuclei for the EC process during infall. In the same figure, the gray lines delimit the isotopic region where experimental values are known for the nuclear masses, and the closed red/blue/green surfaces represents the region where microscopic calculations are available [22,24,25]. The nuclei relevant for EC are essentially located close to the  $N = 50$  shell closure, in good qualitative agreement with the results of the sensitivity study by Sullivan *et al.* [12] and Titus *et al.* [18] (shown by the black contour).

It should be stressed that for most of the 170 different nuclei represented in Fig. 11 no microscopic calculation exists. Dedicated microscopic calculations for all these nuclei represent still an enormous challenge, but it is interesting to observe that these nuclei are concentrated in a relatively reduced zone of the nuclear chart. This means that some

extra experimental and/or theoretical information on weak processes even on a few of the most important ones would greatly help to constrain analytic forms such as ISO, for a systematic application to the whole nuclear pool.

One remark of caution is needed at his point. For our calculations here, we have used the LMP parametrization for all nuclei. This is at variance with Sullivan *et al.* [12], where the LMP was used only for nuclei that are not contained in any of the three tables of Refs. [22,24,25]. The exact list of relevant nuclei for EC might thus be slightly different from those shown in Fig. 11 if the microscopic rates were used where they are known. We expect this effect, however, to be small since most of the relevant nuclei lie outside the range of the tables with microscopic rates. Please note that the absolute rates reported in Fig. 11 are anyway model dependent. For instance, if we had employed the ISO parametrization instead of LMP they would clearly be reduced.

## V. CONCLUSIONS

Within this study we have performed simulations of the prebounce evolution of core-collapse supernovae, investigating the effect of improved EC rates on nuclei developed in Raduta *et al.* [15]. As pointed out already by Langanke *et al.* [26], Bruenn’s EC rates commonly used break down as soon as neutron-rich nuclei become populated abundantly in the later stages of the prebounce evolution. Although some attempts have been made to extent LSSM calculations to heavier and more neutron-rich nuclei using hybrid approaches [11,65], microscopically calculated rates for these nuclei are still not the most convenient to be directly applied in large CCSN simulations. Therefore, for the most exotic and neutron-rich nuclei EC rates are extrapolated [26] and are thus subject to large uncertainties. Sullivan *et al.* [12] have therefore performed a systematic sensitivity study, where individual EC rates were thereby globally scaled by arbitrary factors ranging from 2 to 10 with respect to the fiducial values, showing that the uncertainties on nuclear EC rates have a stronger influence on prebounce evolution than other inputs, such as progenitor model or EoS.

Here, we confirm qualitatively the findings as well of the pioneering work of Hix *et al.* [7], Langanke *et al.* [26], as well as that of Sullivan *et al.* [12] and the subsequent studies of Titus *et al.* [18]. Electron captures occur predominantly on neutron-rich nuclei during the last stages of prebounce, and enhanced captures reduce central  $Y_e$  at bounce with differ-

ences of up to 30% between the different prescriptions for EC on heavy neutron-rich nuclei. Lower  $Y_e$  at bounce leads to smaller inner core mass and slower shock propagation after bounce. The effect of different EC rates is clearly predominant with respect to the EoS, the nuclear mass model, or the progenitor model. However, the improved parametrization ISO motivated by nuclear physics considerations clearly points to a reduction of EC on neutron-rich nuclei with respect to the work by Langanke *et al.* [26]. Although the impact of EC on neutron-rich nuclei is thus attenuated, we emphasize that still the results are considerably different from those employing Bruenn’s rates and it is important to include EC on those nuclei.

The sensitivity to the different prescriptions for EC rates clearly indicates the importance of clarifying the rates on those nuclei, either by theoretical calculations or experiments. Indeed, the parametrization ISO is certainly improved by nuclear physics considerations with respect to the basic extrapolation proposed in LMP, but still it is just an improved fit to complete LSSM calculations, and the differences with respect to the simpler LMP prescription arise from the extrapolation of the fit to the low  $Q$ -value region where no microscopic calculations are available. We have therefore provided a list of the most relevant nuclei, accounting for the 89% of the total time integrated deleptonization rate. Although the details of this list are certainly model dependent (EoS, mass model, progenitor, EC rate parametrization, etc.), there is a large overlap with the 74 most important nuclei for EC identified in Refs. [12,18] with different settings, such that the identification is robust.

Our approach to the computation of EC rates in CCSN simulations presented here possesses the advantages of being numerically efficient and applicable to any EoS. We plan to make public in the near future these rates as well as neutrino-nucleus scattering opacities.

## ACKNOWLEDGMENTS

We would like to thank J. Pons for providing us with the original version of the ACCEPT code, and B. Müller for providing the original version of the fast multigroup transport code. The research leading to these results has received funding from the PICS07889; it was also partially supported by the PHAROS European Science and Technology (COST) Action CA16214 and the Observatoire de Paris through the PTV programme and the action fédératrice “PhyFog.”

- 
- [1] H.-T. Janka, *Annu. Rev. Nucl. Part. Sci.* **62**, 407 (2012).
  - [2] H.-T. Janka, in *Handbook of Supernovae* (Springer, Cham, 2017), p. 1095.
  - [3] H. Bethe, G. Brown, J. Applegate, and J. Lattimer, *Nucl. Phys. A* **324**, 487 (1979).
  - [4] M. B. Aufderheide, I. Fushiki, S. E. Woosley, and D. H. Hartmann, *Astrophys. J. Suppl.* **91**, 389 (1994).
  - [5] A. Heger, K. Langanke, G. Martínez-Pinedo, and S. E. Woosley, *Phys. Rev. Lett.* **86**, 1678 (2001).
  - [6] A. Heger, S. E. Woosley, G. Martínez-Pinedo, and K. Langanke, *Astrophys. J.* **560**, 307 (2001).
  - [7] W. R. Hix, O. E. B. Messer, A. Mezzacappa, M. Liebendörfer, J. Sampaio, K. Langanke, D. J. Dean, and G. Martínez-Pinedo, *Phys. Rev. Lett.* **91**, 201102 (2003).
  - [8] H.-T. Janka, K. Langanke, A. Marek, G. Martínez-Pinedo, and B. Mueller, *Phys. Rep.* **442**, 38 (2007).
  - [9] DUNE Collaboration, [arXiv:1807.10334](https://arxiv.org/abs/1807.10334).
  - [10] C. Kato, H. Nagakura, S. Furusawa, K. Takahashi, H. Umeda, T. Yoshida, K. Ishidoshiro, and S. Yamada, *Astrophys. J.* **848**, 48 (2017).
  - [11] A. Juodagalvis, K. Langanke, W. Hix, G. Martínez-Pinedo, and J. Sampaio, *Nucl. Phys. A* **848**, 454 (2010).

- [12] C. Sullivan, E. O'Connor, R. G. T. Zegers, T. Grubb, and S. M. Austin, *Astrophys. J.* **816**, 44 (2016).
- [13] A. R. Raduta, F. Gulminelli, and M. Oertel, *Phys. Rev. C* **93**, 025803 (2016).
- [14] S. Furusawa, H. Nagakura, K. Sumiyoshi, C. Kato, and S. Yamada, *Phys. Rev. C* **95**, 025809 (2017).
- [15] A. R. Raduta, F. Gulminelli, and M. Oertel, *Phys. Rev. C* **95**, 025805 (2017).
- [16] A. Yudin, M. Hempel, S. Blinnikov, D. Nadyozhin, and I. Panov, *Mon. Not. R. Astron. Soc.* **483**, 5426 (2019).
- [17] H. Nagakura, S. Furusawa, H. Togashi, S. Richers, K. Sumiyoshi, and S. Yamada, *Astrophys. J. Suppl.* **240**, 38 (2019).
- [18] R. Titus, C. Sullivan, R. G. T. Zegers, B. A. Brown, and B. Gao, *J. Phys. G* **45**, 014004 (2018).
- [19] R. Titus, E. M. Ney, R. G. T. Zegers, D. Bazin, J. Belarge, P. C. Bender, B. A. Brown, C. M. Campbell, B. Elman, J. Engel, A. Gade, B. Gao, E. Kwan, S. Lipschutz, B. Longfellow, E. Lunderberg, T. Mijatovic, S. Noji, J. Pereira, J. Schmitt, C. Sullivan, D. Weisshaar, and J. C. Zamora, *Phys. Rev. C* **100**, 045805 (2019).
- [20] A. A. Dzhoiev, K. Langanke, G. Martínez-Pinedo, A. I. Vdovin, and C. Stoyanov, [arXiv:1910.03335](https://arxiv.org/abs/1910.03335).
- [21] G. M. Fuller, W. A. Fowler, and M. J. Newman, *Astrophys. J. Suppl.* **48**, 279 (1982).
- [22] K. Langanke and G. Martínez-Pinedo, *At. Data Nucl. Data Tables* **79**, 1 (2001).
- [23] K. Langanke and G. Martínez-Pinedo, *Rev. Mod. Phys.* **75**, 819 (2003).
- [24] T. Oda, M. Hino, K. Muto, M. Takahara, and K. Sato, *At. Data Nucl. Data Tables* **56**, 231 (1994).
- [25] J. Pruet and G. M. Fuller, *Astrophys. J. Suppl.* **149**, 189 (2003).
- [26] K. Langanke, G. Martínez-Pinedo, J. M. Sampaio, D. J. Dean, W. R. Hix, O. E. B. Messer, A. Mezzacappa, M. Liebendörfer, H. T. Janka, and M. Rampp, *Phys. Rev. Lett.* **90**, 241102 (2003).
- [27] S. Typel, M. Oertel, and T. Klähn, *Phys. Part. Nucl.* **46**, 633 (2015); CompOSE EoS database, <https://compose.obspm.fr>
- [28] H. Dimmelmeier, J. Novak, and P. Cerdá-Durán, CoCoNuT: General relativistic hydrodynamics code with dynamical space-time evolution, Astrophysics Source Code Library, ascl:1202.012, 2012.
- [29] H. Dimmelmeier, J. Novak, J. A. Font, J. M. Ibáñez, and E. Müller, *Phys. Rev. D* **71**, 064023 (2005).
- [30] B. Müller and H. T. Janka, *Mon. Not. R. Astron. Soc.* **448**, 2141 (2015).
- [31] G. Grams, S. Giraud, A. F. Fantina, and F. Gulminelli, *Phys. Rev. C* **97**, 035807 (2018).
- [32] J. V. Romero, J. M. Ibanez, J. M. Martí, and J. A. Miralles, *Astrophys. J.* **462**, 839 (1996).
- [33] J. V. Romero, J. M. Ibáñez, J. A. Miralles, and J. A. Pons, in *Some Topics on General Relativity and Gravitational Radiation*, edited by J. A. Miralles, J. A. Morales, and D. Sáez (Editions Frontieres, Paris, 1997), p. 289.
- [34] A. F. Fantina, Supernovae theory: Study of electro-weak processes during gravitational collapse of massive stars, Ph.D. thesis, Université Paris Sud - Paris XI, 2010, <https://tel.archives-ouvertes.fr/tel-00566480>
- [35] S. E. Woosley, A. Heger, and T. A. Weaver, *Rev. Mod. Phys.* **74**, 1015 (2002); <https://2sn.org/stellarevolution/>
- [36] J. M. Lattimer and F. D. Swesty, *Nucl. Phys. A* **535**, 331 (1991).
- [37] H. Shen, H. Toki, K. Oyamatsu, and K. Sumiyoshi, *Nucl. Phys. A* **637**, 435 (1998).
- [38] J. Lattimer, C. Pethick, D. Ravenhall, and D. Lamb, *Nucl. Phys. A* **432**, 646 (1985).
- [39] M. Hempel, T. Fischer, J. Schaffner-Bielich, and M. Liebendörfer, *Astrophys. J.* **748**, 70 (2012).
- [40] M. Hempel and J. Schaffner-Bielich, *Nucl. Phys. A* **837**, 210 (2010).
- [41] F. Gulminelli and A. R. Raduta, *Phys. Rev. C* **92**, 055803 (2015).
- [42] A. R. Raduta and F. Gulminelli, *Nucl. Phys. A* **983**, 252 (2019).
- [43] S. Furusawa, H. Togashi, H. Nagakura, K. Sumiyoshi, S. Yamada, H. Suzuki, and M. Takano, *J. Phys. G* **44**, 094001 (2017).
- [44] S. Furusawa, K. Sumiyoshi, S. Yamada, and H. Suzuki, *Nucl. Phys. A* **957**, 188 (2017).
- [45] S. Typel, *J. Phys. G* **45**, 114001 (2018).
- [46] S. Typel, G. Röpke, T. Klähn, D. Blaschke, and H. H. Wolter, *Phys. Rev. C* **81**, 015803 (2010).
- [47] P. Moller, J. Nix, W. Myers, and W. Swiatecki, *At. Data Nucl. Data Tables* **59**, 185 (1995).
- [48] E. Chabanat, P. Bonche, P. Haensel, J. Meyer, and R. Schaeffer, *Nucl. Phys. A* **635**, 231 (1998).
- [49] G. Audi, F. Kondev, M. Wang, B. Pfeiffer, X. Sun, J. Blachot, and M. MacCormick, *Chin. Phys. C* **36**, 1157 (2012).
- [50] M. Wang, G. Audi, A. Wapstra, F. Kondev, M. MacCormick, X. Xu, and B. Pfeiffer, *Chin. Phys. C* **36**, 1603 (2012).
- [51] J. Duflo and A. P. Zuker, *Phys. Rev. C* **52**, R23 (1995).
- [52] P. Danielewicz and J. Lee, *Nucl. Phys. A* **818**, 36 (2009).
- [53] BRUSLIB database, <http://www.astro.ulb.ac.be/bruslib/>
- [54] Y. Xu, S. Goriely, A. Jorissen, G. Chen, and M. Arnould, *Astron. Astrophys.* **549**, A106 (2013).
- [55] S. Goriely, N. Chamel, and J. M. Pearson, *Phys. Rev. C* **88**, 024308 (2013).
- [56] G. M. Fuller, W. A. Fowler, and M. J. Newman, *Astrophys. J. Suppl.* **42**, 447 (1980).
- [57] G. M. Fuller, W. A. Fowler, and M. J. Newman, *Astrophys. J.* **252**, 715 (1982).
- [58] G. M. Fuller, W. A. Fowler, and M. J. Newman, *Astrophys. J.* **293**, 1 (1985).
- [59] K. Langanke and G. Martínez-Pinedo, *Nucl. Phys. A* **673**, 481 (2000).
- [60] N. Paar, G. Colò, E. Khan, and D. Vretenar, *Phys. Rev. C* **80**, 055801 (2009).
- [61] Y. F. Niu, N. Paar, D. Vretenar, and J. Meng, *Phys. Rev. C* **83**, 045807 (2011).
- [62] J.-U. Nabi and H. Klapdor-Kleingrothaus, *At. Data Nucl. Data Tables* **71**, 149 (1999).
- [63] J.-U. Nabi and H. V. Klapdor-Kleingrothaus, *At. Data Nucl. Data Tables* **88**, 237 (2004).
- [64] E. Caurier, K. Langanke, G. Martínez-Pinedo, and F. Nowacki, *Nucl. Phys. A* **653**, 439 (1999).
- [65] D. J. Dean, K. Langanke, L. Chatterjee, P. B. Radha, and M. R. Strayer, *Phys. Rev. C* **58**, 536 (1998).
- [66] S. W. Bruenn, *Astrophys. J. Suppl.* **58**, 771 (1985).
- [67] A. Juodagalvis, J. M. Sampaio, K. Langanke, and W. R. Hix, *J. Phys. G* **35**, 014031 (2007).
- [68] Q. Zhi, K. Langanke, G. Martínez-Pinedo, F. Nowacki, and K. Sieja, *Nucl. Phys. A* **859**, 172 (2011).
- [69] J. M. Lattimer, A. Burrows, and A. Yahil, *Astrophys. J.* **288**, 644 (1985).
- [70] A. Burrows and J. M. Lattimer, *Astrophys. J.* **285**, 294 (1984).
- [71] C. J. Horowitz, *Phys. Rev. D* **55**, 4577 (1997).

- [72] S. W. Bruenn and A. Mezzacappa, [Phys. Rev. D](#) **56**, 7529 (1997).
- [73] K. Sumiyoshi, S. Yamada, H. Suzuki, H. Shen, S. Chiba, and H. Toki, [Astrophys. J.](#) **629**, 922 (2005).
- [74] T. Fischer, M. Hempel, I. Sagert, Y. Suwa, and J. Schaffner-Bielich, [Eur. Phys. J. A](#) **50**, 46 (2014).
- [75] J. M. Pearson, R. C. Nayak, and S. Goriely, [Phys. Lett. B](#) **387**, 455 (1996).